Chinese Chemical Letters 35 (2024) 109112

Contents lists available at ScienceDirect

Chinese Chemical Letters

journal homepage: www.elsevier.com/locate/cclet

# Indium-based electrocatalysts for $CO_2$ reduction to C1 products

Qin Cheng[a], Ming Huang[a], Qingqing Ye[a,c], Bangwei Deng[b], Fan Dong[a,b,*]

[a] Research Center for Carbon-Neutral Environmental & Energy Technology, Institute of Fundamental and Frontier Sciences, University of Electronic Science and Technology of China, Chengdu 611731, China
[b] Yangtze Delta Region Institute (Huzhou) & Institute of Fundamental and Frontier Sciences, University of Electronic Science and Technology of China, Huzhou 313000, China
[c] Suzhou Industrial Technology Research Institute of Zhejiang University, Suzhou 215163, China

ARTICLE INFO

*Article history:*
Received 8 May 2023
Revised 24 August 2023
Accepted 16 September 2023
Available online 18 September 2023

*Keywords:*
Electrocatalytic $CO_2$ reduction
In-based catalysts
Formate
Reaction mechanism
Structure-activity relationship

ABSTRACT

Electrocatalytic $CO_2$ reduction at mild conditions is a promising strategy to transform greenhouse gases into fuels or value-added chemicals to solve the increasingly serious environmental and energy problems. The most crucial factor in determining the $CO_2$ reduction performance is to develop efficient electrocatalysts with high selectivity and stability. Among the various electrocatalysts, indium-based catalysts have attracted extensive attention due to their non-toxicity, low cost, and high formic acid/formate selectivity. In this work, we comprehensively review the recent development and research progress of indium-based electrocatalysts for $CO_2$RR. The reaction mechanism, reaction pathways, structure–activity relationship, and strategies to enhance the activity of $CO_2$RR on indium-based catalysts have also been briefly presented and discussed. Finally, the existing challenges and future developments for indium-based high-performance catalysts for $CO_2$RR are proposed.



## 1. Introduction

The significant growing demand for fossil fuel energy resources exacerbates the energy crisis and environmental problems [1–3]. In particular, the global warming and seawater acidification due to the indiscriminate $CO_2$ emissions are becoming more and more serious [4]. To address these energy and environmental problems, use of clean fossil energy with low carbon content, and development of non-fossil energy, such as nuclear energy, hydropower, wind energy, and solar energy would be an alternative route. In addition, converting $CO_2$ gas to high value-added chemicals and/or fuels through development of carbon capture, utilization, and storage (CCUS) techniques has been proposed as one of the most promising strategies to deal with the energy crisis and further achieve carbon neutrality [5].

At present, various techniques have been studied for $CO_2$ conversion, such as photochemistry [6–8], electrochemistry [9–11], thermochemistry [12,13], and biological reduction methods [14]. Among these techniques, electrocatalytic $CO_2$ reduction reaction ($CO_2$RR) has the following advantages: (i) Wide range of renewable electric energy sources, mainly include solar energy, wind energy, tidal energy, and biomass energy [15]; (ii) Mild and controllable reaction conditions; (iii) Compact and modular electrolyzers could be designed for mass production [16]. Using $CO_2$ as a raw material and converting it into value-added fuels or valuable chemicals (CO, HCOOH, $CH_4$, $C_2H_4$, $CH_3CH_2OH$, *etc.*), driven by renewable electricity, is a promising approach to reduce $CO_2$ emission [17–20]. In addition, electrocatalytic $CO_2$RR is gradually becoming mature in terms of fundamental research, theoretical predictions, *in-situ* characterization, and electrolyzer design [21]. In addition, it is in line with the goals of green economy and sustainable development.

However, electrolytic $CO_2$RR on most catalysts usually suffers from unsatisfactory catalytic activity due to the sluggish kinetics of the $CO_2$ activation. In addition, the accompanying hydrogen evolution reaction (HER) is a competing reaction and will decrease the target product selectivity and energy efficiency of $CO_2$RR. Up to now, the low activity, poor product selectivity, undesirable product conversion rate, and catalyst degradation after long-term electrolysis are still the major challenges for the commercialization of electrocatalytic $CO_2$RR [22]. Designing highly efficient and stable electrocatalysts for $CO_2$RR could be a promising route to address these problems. Recently, p-block metal catalysts, including Bi [23–25], Sn [26–28], In [29–35], and Pb [36,37], have been widely studied for electrocatalytic $CO_2$RR, especially for the production of formic acid/formate. Among these p-block metal-based catalysts, indium-based catalyst has attracted great attention due to the following advantages: (i) Indium has abundant resources with relatively

* Corresponding author at: Research Center for Carbon-Neutral Environmental & Energy Technology, Institute of Fundamental and Frontier Sciences, University of Electronic Science and Technology of China, Chengdu 611731, China.
*E-mail address:* dongfan@uestc.edu.cn (F. Dong).

https://doi.org/10.1016/j.cclet.2023.109112
1001-8417/

**Table 1**
Catalytic performances of reported indium-based catalysts for $CO_2$RR.

| Electrocatalyst | Electrolyte | Cell type | Major products | Potential | $FE_{max}$ | Stability test | Current density at $FE_{max}$ (mA/cm$^2$) | Refs. |
|---|---|---|---|---|---|---|---|---|
| Bi-In NPs | 1 mol/L KOH | Flow cell | HCOOH | –0.95 V *vs.* RHE | 92.5% | - | 300 | [39] |
| Cu-In | 0.1 mol/L $KHCO_3$ | H cell | CO | –0.7 V *vs.* RHE | 95% | 7 h | 1.6 | [55] |
| $CuInO_2$ | 0.1 mol/L $KHCO_3$ | H cell | CO | –0.8 V *vs.* RHE | 70% | 5 h | - | [56] |
| Cu/In nanoparticles | 0.1 mol/L $KHCO_3$ | H cell | CO | –0.7 V *vs.* RHE | 79.7% | - | - | [57] |
| $Cu_{11.5}In_{88.5}$-OH | 0.1 mol/L $KHCO_3$ | H cell | HCOOH | –1.01 V *vs.* RHE | 85% | 10 h | - | [58] |
| Cu-In (80 at%In) | 0.1 mol/L $KHCO_3$ | H cell | HCOOH | –1.0 V *vs.* RHE | 62% | - | ~0.72 | [59] |
| $SnInO_x$ | 0.1 mol/L $KHCO_3$ | H cell | HCOOH | –1.0 V *vs.* RHE | 80% | 10 h | 24 | [62] |
| In–Sn alloy | 0.1 mol/L $KHCO_3$ | H cell | HCOOH | –1.2 V *vs.* RHE | 86% | 12 h | 9.6 | [32] |
| In-doped SnOx | 1 mol/L $KHCO_3$ | Flow cell | HCOOH | –0.98 V *vs.* RHE | 94% | 12 h | 236 | [63] |
| $In^{\delta+}$-$N_4$ | 0.5 mol/L $KHCO_3$ | H cell | HCOOH | –0.65 V *vs.* RHE | 96% | 60 h | 8.87 | [79] |
| In–$N_3$–V | 0.5 mol/L $KHCO_3$ | H cell | CO | –0.57 V *vs.* RHE | 95% | 14 h | ~2.3 | [78] |
| In-SACs | 0.5 mol/L $KHCO_3$ | H cell | CO | –0.6 V *vs.* RHE | 97% | 60 h | ~4 | [77] |
| $In_A$/NC | 0.5 mol/L [Bmim]$PF_6$/MeCN | H cell | CO | –2.1 V *vs.* Ag/AgCl | 97.2% | 24 h | 39.4 | [70] |
| In–N–C | 0.5 mol/L $KHCO_3$ | H cell | HCOOH | –0.79 V *vs.* RHE | 80% | 20 h | 6.8 | [80] |
| InNi DS/NC | 0.5 mol/L $KHCO_3$ | H cell | CO | –0.7 V *vs.* RHE | 96.7% | 39 h | ~14 | [83] |
| $In_2O_3$ nanocrystal | 0.5 mol/L $KHCO_3$ | H cell | HCOOH | –1.0 V *vs.* RHE | >90% | 12 h | 11.4 | [88] |
| $In_2O_3$-rGO | 0.1 mol/L $KHCO_3$ | H cell | HCOOH | –1.2 V *vs.* RHE | 84.6% | 10 h | 22.5 | [89] |
| $In_2O_3$-PVDF | 0.5 mol/L $KHCO_3$ | H cell | HCOOH | –0.67 V *vs.* RHE | 82.4% | | ~3 | [33] |
| In@CNR | 0.5 mol/L $KHCO_3$ | H cell | HCOOH | –0.86 V *vs.* RHE | 92.3% | 12 h | 11 | [90] |
| H-$InO_x$ NRs | $NaHCO_3$ | H cell | HCOOH | –0.7 V *vs.* RHE | 91.7% | 20 h | ~5 | [91] |
| S-In | 0.5 mol/L $KHCO_3$ | H cell | HCOOH | –0.98 V *vs.* RHE | 93% | 1 h | ~60 | [94] |
| $In_2O_3$/InN | 0.1 mol/L $KHCO_3$ | H cell | HCOOH | –1.48 V *vs.* RHE | 95.7% | 30 h | 17.7 | [96] |
| In/$In_2O_3$ | 0.5 mol/L $KHCO_3$ | H cell | HCOOH | –1.0 V *vs.* RHE | 91% | 12 h | ~25 | [97] |
| InN | 1 mol/L KOH | Flow cell | HCOOH | –0.9 V *vs.* RHE | 91% | 3 h | 30.0 | [101] |
| $In_2S_3$–RGO | 0.1 mol/L $KHCO_3$ | H cell | HCOOH | –1.2 V *vs.* RHE | 91% | 6 h | ~6.5 | [98] |
| $In_2Se_3$ | 0.1 mol/L $KHCO_3$ | H cell | CO | –0.7 V *vs.* RHE | 89% | 24 h | - | [100] |
| In/$In_2O_{3-x}$ | 0.5 mol/L $NaHCO_3$ | H cell | HCOOH | –0.82 V *vs.* RHE | 89.2% | 10 h | - | [34] |
| Indium/Indium Oxide | 0.5 mol/L $KHCO_3$ | H cell | HCOOH | –0.82 V *vs.* RHE | 90% | 25 h | ~6 | [35] |
| V–doped $In_2O_3$ | 0.1 mol/L $KHCO_3$ | H cell | $CH_3OH$ | –0.83 V *vs.* RHE | 15.8% | - | - | [95] |

low cost; (ii) Indium is a non-toxic element with easy processing feature; (iii) Excellent physical and chemical properties, such as good electrical conductivity and the property of easily forming alloys with other metals [38]; (iv) High selectivity to the production of formic acid: In has a high binding energy to *HCOO, which favors the conversion of $CO_2$ to HCOOH [39]. Up to now, various indium–based catalysts including metal structures, alloys, oxides/hydroxides, nitrides, sulfides, clusters, single-atoms, and their composites with carbon materials have been intensively synthesized and used for electrolytic $CO_2$RR (Table 1). The catalyst types, dimensions, morphologies, defects, surface properties, and electrochemical cells all show significant influences on the final performance of $CO_2$RR. To date, a few review articles have been focused on the development of metal–based $CO_2$RR electrocatalysts [40–43]. However, a timely and comprehensive review on the design and development of indium-based electrocatalysts for electrolytic $CO_2$RR is still lacking.

Herein, the recent development of indium-based electrocatalysts in electrolytic $CO_2$RR to C1 products is systematically summarized and discussed. The rational design of indium-based catalysts, including structure, composition, morphology, and single-atom structure, has been proven to be effective in promoting the electrolytic $CO_2$RR performance (Fig. 1). We first briefly introduce the possible reaction pathways for the $CO_2$RR on indium-based electrocatalysts surface. Then we present the design strategies of various types of indium-based electrocatalysts with high performance, including the modulation of dimension, size, morphology, composition, single-atom structure, defect, heterostructure, and some other catalysts. Finally, the remaining challenges and future development in this field are envisioned.

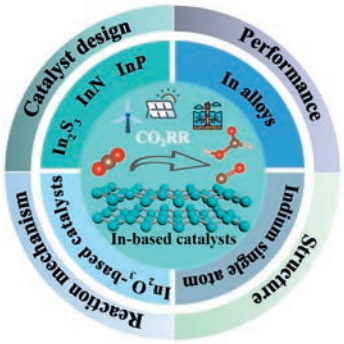


**Fig. 1.** Summary of In-based catalyst design strategies for highly efficient electrolytic $CO_2$RR.

## 2. Reaction pathways of $CO_2$RR on indium-based electrocatalysts

It is generally known that the formation of products in electrolytic $CO_2$RR mainly includes three steps: $CO_2$ adsorption on catalysts surface, the transfer of electrons/protons to the absorbed $CO_2$ molecules, and desorption of product molecules from catalyst surface. The reaction products of $CO_2$ on indium-based catalysts are mainly formate or CO, which is a typical two electrons/protons transfer process. The product selectivity largely depends on the first proton coupling process on the catalyst surface. In other words, whether the first proton is added to the C atom or the O atom in the activated $CO_2^-$, determining the formation of different products. At present, a large number of studies suggest that the $CO_2$RR on indium-based catalysts surface usually has three pathways (Fig. 2) [44–47], which including (i) the two oxygen atoms in $CO_2^-$ are bound to the catalyst surface, and the carbon atom is protonated to generate the HCOO* intermediate, which follows by a second electron transfer and protonation process to form HCOOH [4]; (ii) unlike the former, *OCHO intermediate should be formed through an electron transfer process of the as-formed HCOO* intermediate, which will be further protonated to form HCOOH [47]; (iii) different from the previous two pathways, the C atom in $CO_2^-$ may also be bonded to the catalyst surface. In this case, one of the oxygen atoms will be protonated to

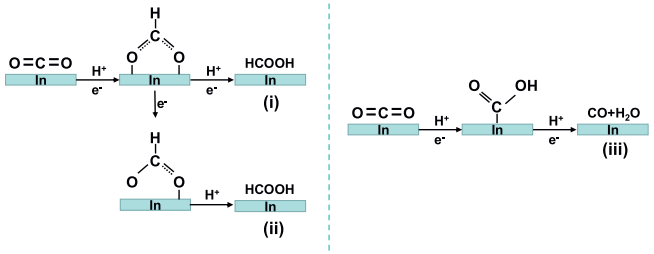


**Fig. 2.** Possible reaction pathways of electrolytic $CO_2$RR on the surface of indium-based electrocatalyst.

form a COOH* intermediate, following by an electron transfer and protonation process and a further dehydration to form CO [11].

## 3. Advanced indium-based catalysts for high-performance electrolytic $CO_2$RR

### 3.1. In-based alloys

Alloying is a common and efficient approach to improve the activity and selectivity for electrolytic $CO_2$RR. Attributing to the altered composition, electronic structure, and surface properties (such as varied electronegativity, undercoordinated active sites, surface atom distribution, and lattice mismatch), alloys show tunable catalytic activity compared to pure metals [48–50]. Until now, numerous studies have shown that the combination of binary metal elements with different electronic properties can significantly adjust the surface chemical environment and the adsorption energy of reaction intermediates during $CO_2$RR. Many indium-based alloys have been reported for electrolytic $CO_2$RR, however, unlike Sn and Bi, indium-based alloys are more likely to enhance the selectivity of CO [51–54].

#### 3.1.1. Cu-In alloy

Among the numerous bimetallic catalysts, Cu-In alloys have attracted great attention due to the unique electronic structure of Cu. Rasul *et al.* electrodeposited In on rough Cu surface to a Cu-In alloy catalyst, exhibiting a Faraday efficiency of 95% for $CO_2$-to-CO conversion at a potential of –0.7 V *vs.* RHE. The Faraday efficiency of CO can be maintained at 85% after electrolysis for 7 h (Figs. 3a and b) [55]. The theoretical calculations show that the introduction of In does not change the electronic properties of Cu, but In preferentially locates at the edge of Cu, which can stabilize the reaction intermediate (COOH*) and further promote the reduction of $CO_2$ to CO (Fig. 3c). Moreover, Rasul and his group members reported the construction of Cu-In alloy interface during electrolysis process of $CO_2$RR when using $CuInO_2$ as the starting catalyst (Figs. 3d and e) [56]. The as-formed Cu-In catalyst shows a formate selectivity of 31% selectivity and a CO selectivity of 63% selectivity with suppressed HER. Theoretical calculations reveal that In occupies the stepped sites of Cu, and does not show a preferential adsorption of H* or CO* intermediates. While the vicinal Cu affects the adsorption of H* or CO* intermediates, and the synergistic effect of In and Cu finally attributes to the selectivity of electrolytic $CO_2$RR (Figs. 3f and g). These studies indicate that the introduction of two metals with different properties at the two-phase interface can change the adsorption strengths of reaction intermediates, thereby changing/enhancing the selectivity of target products.

Apart from the formation of alloy interface, recent studies revealed the promotion of electrolytic $CO_2$RR by tuning the structure and composition of Cu-In alloy. For example, by controlling the annealing temperature, Shen *et al.* prepared various Cu-In bimetallic catalysts with different structures (hollow spheres and double-layer hollow spheres) and different phases (CuO and $Cu_2O$) for $CO_2$ reduction to syngas (CO and $H_2$) [57]. The authors found that the structure and phase of catalysts during the $CO_2$RR process determines the formation of syngas with different compositions (Fig. 4a). After the introduction of In into Cu, the Faradaic effi-

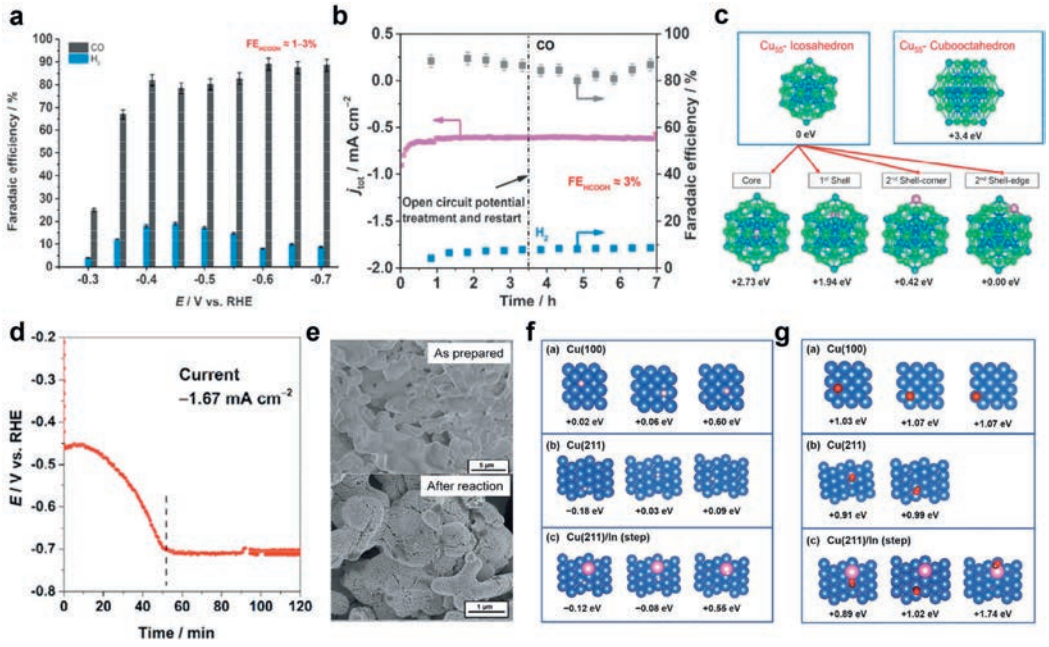


**Fig. 3.** (a) Faradaic efficiencies for CO and $H_2$ on Cu-In alloys at different potentials. (b) Long-term stability test for Cu-In alloy at a potential 0.6 V *vs.* RHE. (c) Site preference of In in $Cu_{55}$-Icosahedron cluster and $Cu_{55}$-Cubooctahedron cluster. The energies relative to $Cu_{55}$-Icosahedron are shown. Reproduced with permission [55]. Copyright 2015, Wiley-VCH Verlag GmbH & Co. KGaA. (d) Chronopotentiometric test of $CuInO_2$ catalyst at a current density of –1.67 mA/cm$^2$. (e) SEM images of Cu-In electrodes before and after electrolysis. Optimized geometries and relative adsorption energies of H (f) and CO (g) on Cu (100), Cu (211), and In-modified (211) Cu facet. Reproduced with permission [56]. Copyright 2015, The Royal Society of Chemistry.

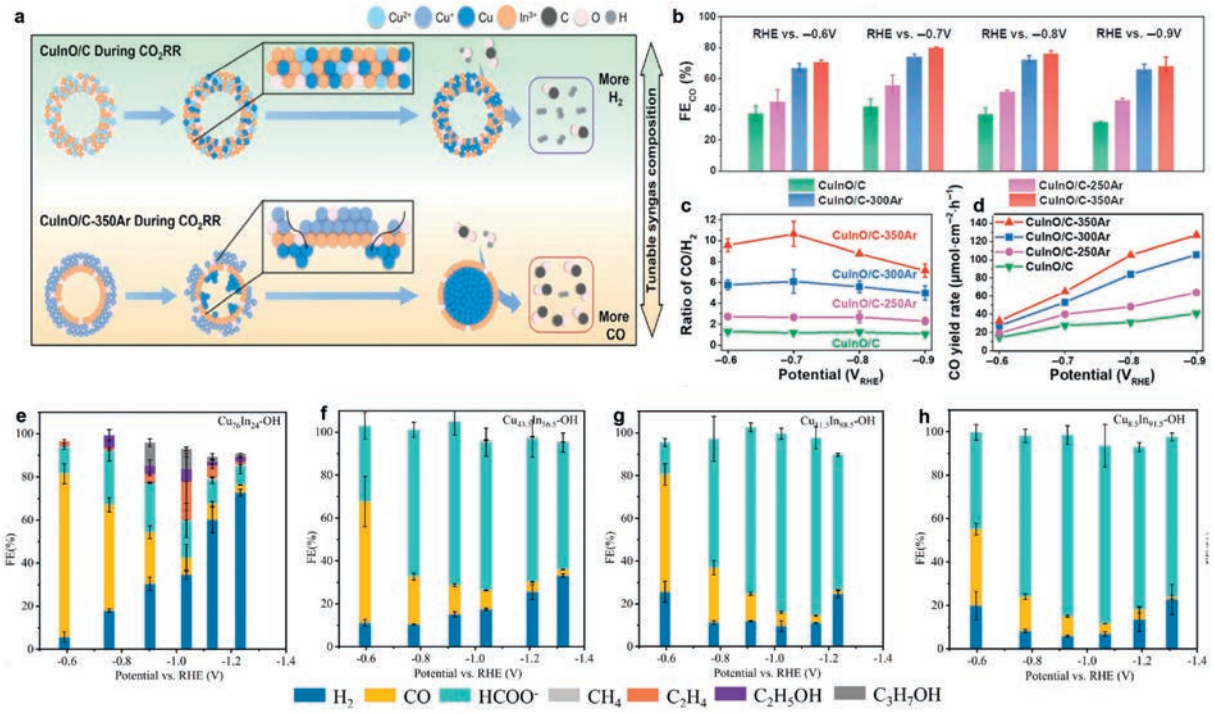


**Fig. 4.** (a) Illustration shows the surface evolution of Cu-In based catalysts during $CO_2$RR and the varying product selectivity. (b-d) Evaluation of $CO_2$RR performance on various catalysts. Reproduced with permission [57]. Copyright 2021, Springer. Faradaic efficiencies for various products on $Cu_xIn_y$ hydroxide catalysts: (e) $Cu_{76}In_{24}$-OH, (f) $Cu_{43.5}In_{56.5}$-OH, (g) $Cu_{11.5}In_{88.5}$-OH, (h) $Cu_{8.5}In_{91.5}$-OH. Reproduced with permission [58]. Copyright 2021, Elsevier.

ciency of CO and the syngas yield increase at all potentials with increasing annealing temperature in Ar (Figs. 4b–d). In addition, the atomic composition of Cu-In alloy directly affects product selectivity during $CO_2$RR. Xie and colleagues synthesized Cu-In hydroxides ($Cu_xIn_y$-OH) with tunable compositions by a simple hydrothermal method, and they found that the selectivity of products shifted from CO to formic acid when the In content was increased (Figs. 4e–h) [58]. Similarly, Hoffman's group also demonstrated that the selectivity of target product could be controlled by altering the alloy composition [59]. Therefore, by controlling the structure and composition of the catalyst for $CO_2$RR, the selectivity of the product can be directionally improved or regulated [60,61].

### 3.1.2. Sn-In alloy

Sn and In exhibit similar features in electrocatalytic $CO_2$RR with high selectivity for formate, and the Sn-In alloy is expected to enhance this selectivity to some extent. Pardo Pérez and his coworkers reported the formation of metal/metal oxide core-shell nanoparticles *via* an *in situ* reduction of the amorphous $SnInO_x$ film during electrocatalytic process [62]. Their results show that the *in situ* reduced $Sn_{1-X}In_X$@$In_{1-Y}$ was composed of Sn-rich SnIn alloy nanocore and $InO_x$-rich $SnInO_x$ shell (Figs. 5a–d). Consequently, the *in-situ* formed catalyst had a Faradaic efficiency of 80% for formate without significant degradation under electrolysis for up to 10 h (Fig. 5e). Wang group prepared Sn-In core-shell nanoparticles with an $InSn_4$ core and an amorphous In-doped tin oxide shell *via* a one-step method [63]. They found that the content of indium in the Sn-In alloy plays an important role in determining the activity and Faradaic efficiency of $CO_2$ reduction to formate. The best $CO_2$ reduction performance was achieved when the content of In was 30% (Fig. 5f). Theoretical calculations and X-ray absorption near edge structure (XANES) spectra show that In doping in $SnO_2$ shell results in the generation of oxygen vacancies, promoting the production of formic acid while suppressing hydrogen evolution (Fig. 5g). This core@shell structure can tune $CO_2$RR selectivity through synergistic effect between core-shell components, which offers potential advantages for electrocatalysis [26,64].

### 3.1.3. Bi-In alloy

Bi-In alloy has also been recognized efficient catalyst for the electroreduction of $CO_2$ to formic acid with high selectivity. For instance, Yao *et al.* reported the synthesis of BiIn alloy nanoparticles using bimetallic metal-organic frameworks as precursors, which exhibited a HCOOH Faradaic efficiency of 92.5% at the current density of 300 mA/cm$^2$. Remarkably, long-term stability for HCOOH production was achieved with the FE > 80% at the current density of 120 mA/cm$^2$ in the MEA system for 25 h [39]. Tan *et al.* prepared the indium−bismuth nanosphere ($In_{16}Bi_{84}$ NS) *via* a facile liquid-polyol technique. The as-synthesized $In_{16}Bi_{84}$ NS exhibited ~100% formic acid faradaic efficiency at −1.4 V *vs.* RHE, and the FE could be maintained > 90% in a wide potential window (−0.84 to −1.54 V *vs.* RHE) [65]. The excellent catalytic performance was ascribed to the modulated electronic properties from the synergistic effect of In and Bi, enhancing the adsorption of the intermediate (HCOO*) on the catalyst surface to favor the formation of formic acid. Xiong *et al.* presented the controlled synthesis of bimetallic $Bi_xIn_y$ nanofiber catalysts with 3D network structure *via* an electrospinning process followed by electrochemical reduction. The obtained $Bi_5In_5$ nanofiber catalyst achieved a maximum $FE_{formate}$ of 96.8% with a production rate of ~4.55 mmol h$^{-1}$ cm$^{-2}$. The enhanced $CO_2$RR performance was attributed to the large specific surface area and exposure of the InBi (200) plane, which has high reactivity and selectivity for formate [38].

### 3.1.4. Other In-based alloys

Apart from the In-based alloy with p-block metals and transition metals, some noble metals can also form alloys with In for

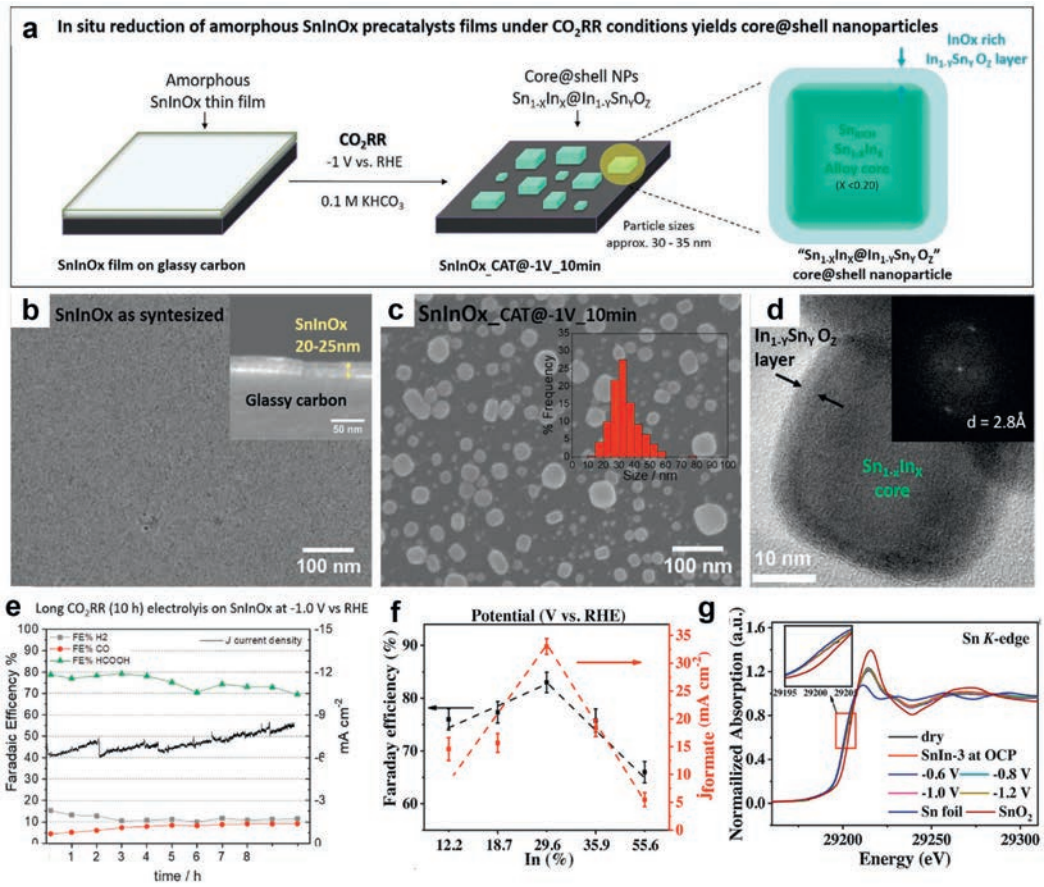


**Fig. 5.** (a) Schematic illusation of the *in situ* conversion of $SnInO_x$ film to $Sn_{1-X}In_X@In_{1-Y}Sn_YO_Z$ core@shell nanoparticles. (b) SEM image of synthesized $SnInO_x$ planar film (inset is a cross-sectional SEM image). (c) SEM image of the $SnInO_x$ film after $CO_2RR$ for 10 min. (d) TEM image of $SnInO_x$_CAT@-1V_10 min (inset shows the corresponding FFT image). (e) Long-term stability of untreated $SnInO_x$ after electrolysis at −1.0 V for 10 h. Reproduced with permission [62]. Copyright 2021, Wiley-VCH GmbH. (f) The dependence of $FE_{formate}$ and $j_{formate}$ on the indium content in Sn-In alloy nanoparticles at −1.0 V *vs.* RHE. (g) Sn K-edge XANES spectrum of SnIn alloy nanoparticles at different potentials. Reproduced with permission [63]. Copyright 2021, Elsevier.

electrocatalytic $CO_2RR$. It is known that Ag-based catalysts show good selectivity to CO in $CO_2RR$, and combining Ag with In to form a bimetallic alloy can further improve the $CO_2RR$ performance. Larrazábal *et al.* deposited Ag nanoparticles on $In_2O_3$ and $In(OH)_3$ which was further transformed into Ag-In alloy during the electrolysis process [66]. Their experiments show that the Ag contents and the support catalysts both could affect the selectivity of CO, depending on the exposure of real active sites during electrolysis. It's also noting that the introduction of In into Pd catalyst to form an In-Pd alloy can suppress the CO poisoning problem in the pure Pd catalyst to a certain extent and further improve the CO selectivity [67].

Compared with monometallic catalysts, bimetallic alloy catalysts are composed of two different elements, which, to a certain extent, could change or modulate the electronic structure and geometry of active sites on catalyst surface. The catalyst electronic structure directly affects the binding with reaction intermediates and the reaction pathways. Changes in the geometry affects the local atomic arrangement of the active site, which could favor the formation of certain intermediates and effectively alter the reaction pathway. Thus, the alloying process could enhance the adsorption and activation capabilities of the catalyst, further improving the overall performance of the catalyst [50,68]. On the other hand, the introduction of another element into the indium-based catalyst to form an In-based alloy could realize the regulation of product selectivity. Although alloying can increase product diversity, the Faradaic efficiency for individual product may decrease compared to bare indium catalysts. Thus, the future research in this field needs rational design of the structure, components, and composition of the In-based alloy to exert the role of the two components to maximize the synergistic effect to produce the target product.

### 3.2. Atomically dispersed catalysts

#### 3.2.1. In single atomic catalysts

Single-atom catalysts (SACs) have attracted extensive attention due to their full atom utilization efficiency and excellent catalytic performance. P-block metals (Bi [69], In [70], Sn [71]), transition metals (Fe [72], Ni [73], Zn [74]), and noble metals (Ag [75], Pd [76]) all have been used to construct single-atom catalysts. Ni SACs were the most widely used catalyst in $CO_2RR$ research. Recently, In SACs have also been reported for electrocatalytic $CO_2RR$ due to their excellent $CO_2$ catalytic activity.

Zhang *et al.* prepared a series of In-$N_xC_{4-x}$ ($1 \leq x \leq 4$) single-atom catalysts *via* a pyrolysis process for $CO_2$ reduction to CO [77]. It was found that the dominate product on $In_2O_3$ NPs catalyst is formate with a small amount of CO. While the reduction product on In SACs is transformed into CO, indicating the regulation of product selectivity on indium-based catalysts (Fig. 6a). Theoretical calculations simulated the adsorption configurations and evolution processes of catalysts with small molecules, and the results showed that the change of the product from formate to CO on the

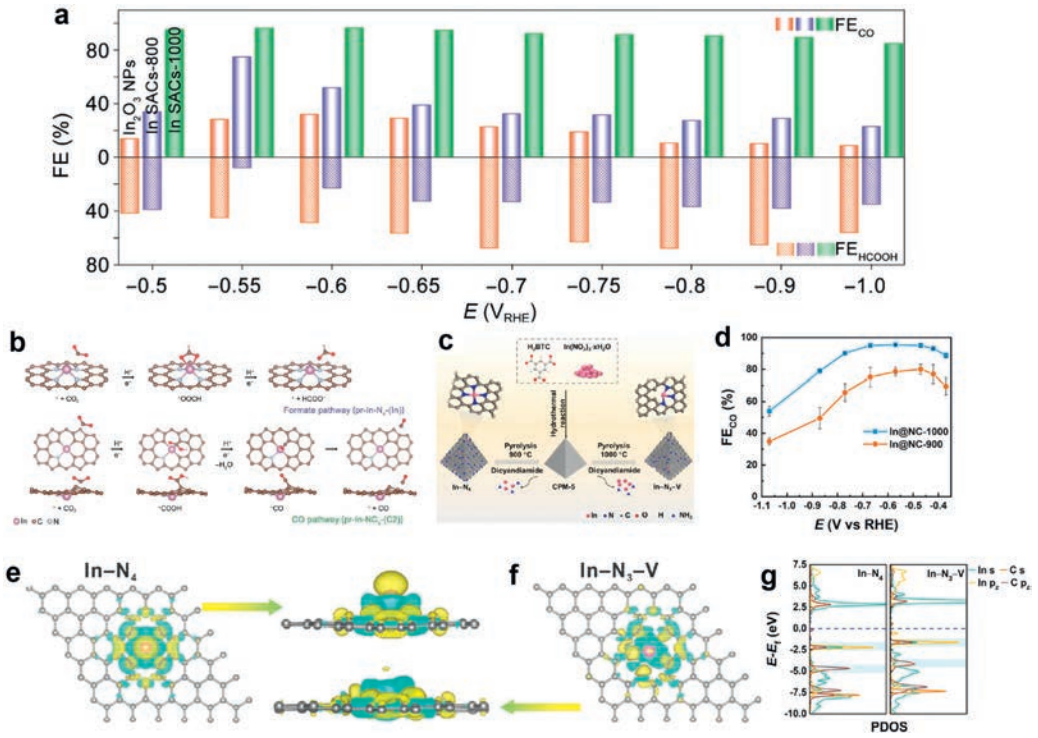


**Fig. 6.** (a) Product selectivity of $In_2O_3$ and InSA catalysts at different potentials. (b) Proposed reaction pathways of $CO_2$RR on pr-In-$N_4$-(In) and pr-In-$NC_3$-(C2). Reproduced with permission [77]. Copyright 2022, Springer Nature. (c) Schematic illustration showing the prepration of In-$N_3$-V SACs. (d) $FE_{CO}$ at various potentials for In@NC-900 and In@NC-1000. (e, f) Calculated charge density for In−$N_4$ and In−$N_3$−V catalytic centers (yellow iso-surfaces represent depletion and blue iso-surfaces represent gain of electron density. An iso-surface value was set at 0.001 e/Å$^3$). (g) PDOS of In (s and $p_z$ orbitals In−$N_4$ and In−$N_3$−V) with C (s and $p_z$ orbitals in COOH*). Reproduced with permission [78]. Copyright 2022, American Chemical Society.

In SACs is due to the transfer of the real active site from pure metallic In center to the adjacent carbon atom coordinated by the In atom (Fig. 6b). Beside, In SACs can also affect the formation energies of reaction intermediates by adjusting the hybridization energy levels. Li and his collaborators proposed two types of In SACs: four nitrogen atoms-coordinated (In-$N_4$) SAC and three nitrogen atoms-coordinated with a vacancy (In-$N_3$-V) SAC (Fig. 6c) [78]. Notably, In-$N_3$-V catalyst exhibits a CO Faradaic efficiency ($FE_{CO}$) of 95%, which is much higher than that of In-$N_4$ catalyst with a maximum $FE_{CO}$ of 80% (Fig. 6d). Theoretical calculations were further performed to investigate the intrinsic relationship between SAC structure and performance. Compared with In-$N_4$, the In atoms in In-$N_3$-V are much easier to enrich electrons, and the vacancy makes the s and $p_z$ orbital energies of In atoms closer to the Fermi level, thereby reducing the formation energy of COOH* and improving catalytic performance (Figs. 6e–g). The selectivity of $CO_2$RR products can be effectively tuned by regulation of the catalytic active sites and atomic structure of In SACs. In this regard, revealing the intrinsic relationship between the structure and catalytic property of SACs provides guidance for rational design of electrocatalysts.

Even CO was the mostly reported reduction product on In SACs, formic acid/formate has also been achieved on the In-based SACs. For example, Shang *et al.* synthesized $In^{\delta+}$-$N_4$ SACs through wet-impregnation and pyrolysis, exhibiting a $FE_{formate}$ of 96% at the potential of –0.65 V *vs.* RHE and a turnover frequency (TOF) of 12500 h$^{-1}$ at –0.95 V *vs.* RHE [79]. In addition, Liu and his collaborators demonstrated that In single atoms supported on carbon substrates (In-N-C) can effectively improve the electrocatalytic performance of $CO_2$ reduction reaction, and the *OCHO intermediate formed at atomically dispersed In sites directly determine the formation of formate [80]. Due to the relatively simple coordination environment and well-defined active sites of In single atoms, the adsorption strength of intermediates can be effectively modulated by adjusting the coordination environment, thereby determining the product selectivity.

### 3.2.2. *In-based diatomic catalysts*

Although single-atom catalysts have high atom utilization efficiency, they still suffer from simple structures and lack of cooperative active sites, which limits their application in some complex reactions [81]. To solve this problem, single-atom catalysts with dual metals (diatomic catalysts) have been rationally designed. Yuan *et al.* prepared Cu-In diatomic catalyst by the pyrolysis of CuIn metal-organic framework (MOF). The Cu-In diatomic catalyst shows high selectivity for $CO_2$RR to methanol, which is higher than that of pure copper single-atom catalysts [82]. The Cu-In dual atomic sites were proved to effectively hinder the hydrogen evolution reaction and promote the conversion of $CO_2$ to methanol due to the synergistic effect between Cu and In. Fan and coworkers designed a dual-site atomic In-Ni catalyst anchored on nitrogenated carbon (InNi DS/NC). The InNi DS/NC has an excellent CO selectivity > 90% over a wide potential range (−0.5 to −0.8 V *vs.* RHE). *In situ* ATR-SEIRAS and theoretical calculations reveal that the In-Ni diatomic active sites and the O atom bridge cannot only lower the reaction energy barrier of *COOH but also suppress hydrogen evolution, promoting the $CO_2$RR performance [83]. In addition, atomically dispersed In-Ce diatomic catalysts on nitrogen-doped carbon (In-Ce/CN) have also prepared for $CO_2$ reduction to formic acid [84]. The introduction of Ce single atomic sites cannot only significantly promote the electron transfer during the reaction process but also optimize the In-5p orbitals, favoring the formation of. It is apparent that the two adjacent separated active sites in diatomic catalysts can provide two absorption sites and act as synergistic sites to improve catalytic activity as compared to the bare single-atom catalysts [85].

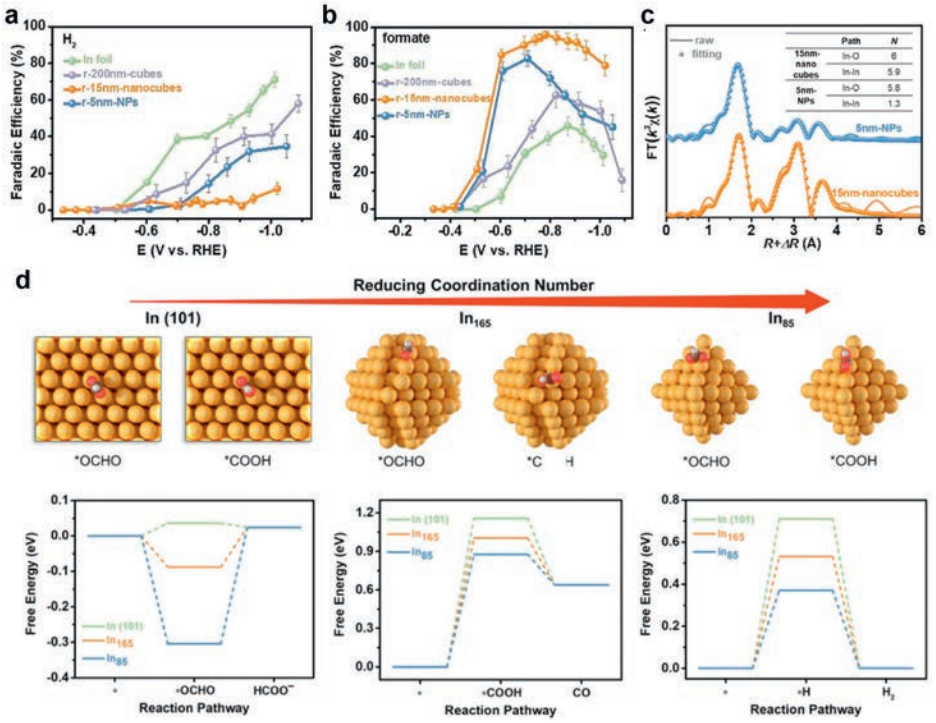


**Fig. 7.** Faradaic efficiencies for $H_2$ (a) and Faradaic efficiencies for formate (b) of different catalysts at various potentials. (c) EXAFS spectra and corresponding fitting curves for 5 nm-NPs and 15 nm-nanocubes (inset is a table showng the fitting parameters). (d) Optimized configurations of *OCHO and *COOH absrobed on In (101), $In_{165}$, and $In_{85}$ surface, and the Gibbs free energy diagrams for the formation of $HCOO^-$, CO and $H_2$. Reproduced with permission [88]. Copyright 2021, Wiley-VCH GmbH.

### 3.3. Indium oxide-based catalysts

#### 3.3.1. $In_2O_3$

$In_2O_3$ is also a typical catalyst in $CO_2$RR, and many studies have shown that the structure engineering of $In_2O_3$ is an effective way to enhance the $CO_2$RR performance [86,87]. Understanding the correlation between structure and catalytic performance of catalysts is of great importance. Firstly, the size or dimension of catalyst shows a significant influence in the catalytic reaction. The size engineering of the catalyst not only can affect the specific surface area but also can tune the local electronic structure of the catalyst, showing a critical role in determining the catalytic performance. To prove this point, Huang *et al.* prepared 5 nm $In_2O_3$ nanoparticles (NPs) and 15 nm $In_2O_3$ nanocubes by a solvothermal reaction [88]. Compared with 200 nm $In_2O_3$ cubes and 5 nm $In_2O_3$ NPs, 15 nm $In_2O_3$ nanocubes possessed highest formate Faradaic efficiency (>95%) and negligible side reactions with a smallest overpotential (Figs. 7a and b). Fourier-transform extended X-ray absorption fine structure (EXAFS) spectroscopy reveals that the coordination numbers of In decreases with the decrease of the size (Fig. 7c). Moreover, theoretical calculations simulated the $In_2O_3$ models with three different particle sizes. The free energy diagrams for the formation of reaction intermediates show that size reduction (coordination deficiency) is beneficial for the adsorption of all three intermediates (*OCHO, COOH*, and H*) (Fig. 7d), but the H* adsorption free energy gradually approaches the thermoneutral as the catalyst size shrinks down, indicating that HER becomes more competitive at smaller sizes. This also agrees with the experimental result that 5 nm $In_2O_3$ shows higher $H_2$ selectivity (lower formate selectivity) than 15 nm $In_2O_3$. This study provides a new perspective on the structure-property relationship of indium-based catalysts: the size engineering of the catalyst does not necessarily mean that the smaller the better.

Except the size engineering, combining indium-based oxides with conductive carbon substrates to form hybrid materials (with potential chemical coupling between different components) is another effective route to modulate the $CO_2$RR performance. For example, Zhang and coworkers revealed the role of chemical interactions between $In_2O_3$ and reduced graphene oxide (rGO) in promoting the $CO_2$RR (Fig. 8a) [89]. In their work, porous $In_2O_3$ nanobelts were uniformly grown on reduced graphene oxide (Fig. 8b). Compared with the physically mixed $In_2O_3$-rGO catalyst, the Faradaic efficiency and partial current density of chemically bonded $In_2O_3$-rGO hybrid catalyst for formate formation were increased by 1.4 times and 3.6 times, respectively. Further, charge distribution and Gibbs free energy diagrams revealed that the strong chemical coupling between $In_2O_3$ and rGO could enhance electric conductivity and reduce the formation energy of reduction intermediates (HCOO*), thus promoting the electrolytic $CO_2$RR activity (Figs. 8c and d). In addition, $In_2O_3$ nanoparticles dispersed on conductive carbon nanorods achieved a $FE_{formate}$ of 90% and the catalyst also delivered a high current density of 300 mA/cm$^2$ when applied to a gas-diffusion electrode-based flow cell [90].

Oxygen vacancy engineering to modulate the electronic structure of $In_2O_3$ is also an effective strategy to improve the $CO_2$RR performance. Zhang and his team synthesized $InO_x$ nanobelts with three different concentrations of oxygen vacancies, in which the highest oxygen concentration leads to the best electrolytic $CO_2$RR performance (Figs. 8e–g) [91]. Cheng *et al.* synthesized $In_2O_3$ nanorods with different oxygen vacancy concentrations through an annealing atmosphere-assisted strategy for efficient electrocatalytic $CO_2$ reduction to produce formate (Figs. 9a and b) [92]. A combination of XPS, EPR, and XAFS techniques revealed the successful tuning of oxygen vacancy concentration in $In_2O_3$ (Figs. 9c–e). Notably, the introduction of oxygen vacancies significantly enhanced the conversion activity and selectivity of $CO_2$RR to formate (Fig. 9f). DFT calculations show that oxygen vacancies can significantly promote the interaction between HCOO* intermediates and In atoms and lower the energy barrier for the formation of HCOO*, lead-

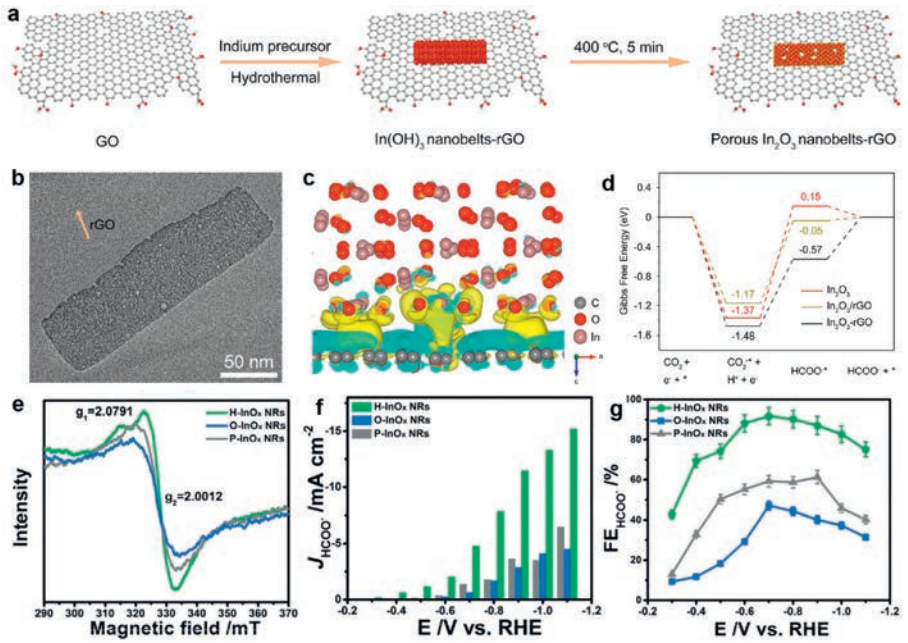


**Fig. 8.** (a) Schematic shows the preparation of porous $In_2O_3$−rGO hybrid structure. (b) TEM image of porous $In_2O_3$−rGO hybrid structure. (c) Calculated differential charge diagram for $In_2O_3$−rGO hybrid catalyst. (d) Gibbs free energy diagrams for $CO_2$-to-formate on different catalysts. Reproduced with permission [89]. Copyright 2019, American Chemical Society. (e) Electron paramagnetic resonance (EPR) spectra of three InOx samples. Partial current density (f) and Faradaic efficiency (g) of $HCOO^-$ on three $InO_x$ samples. Reproduced with permission [91]. Copyright 2019, Wiley-VCH Verlag GmbH & Co. KGaA.

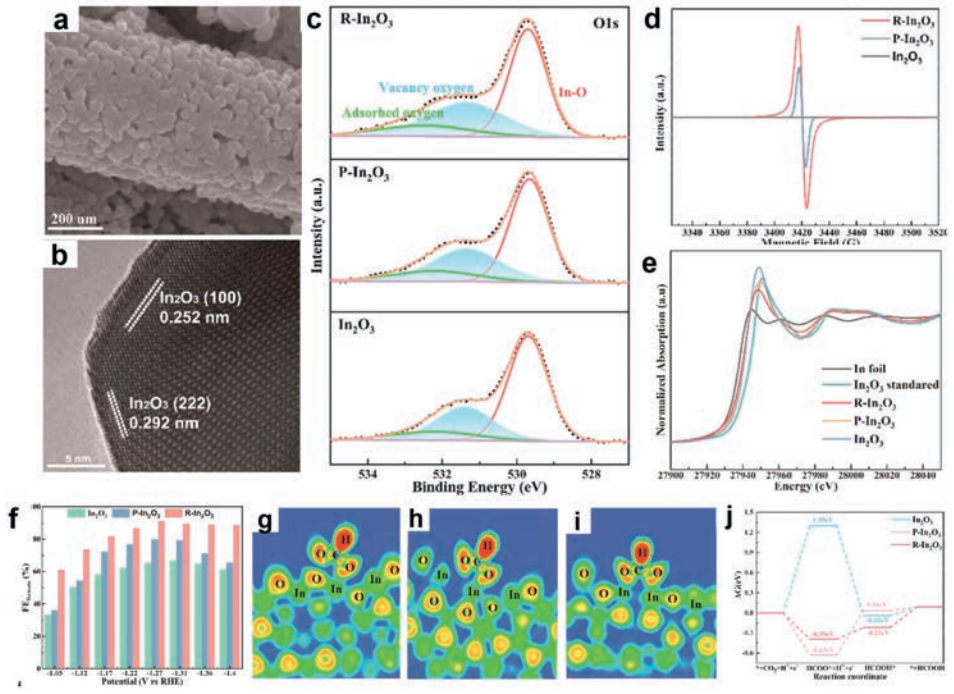


**Fig. 9.** (a) A typical SEM image of oxygen vacancy-rich $In_2O_3$ catalyst (R-$In_2O_3$). (b) HRTEM image of R-$In_2O_3$. (c) O 1s XPS spectra of $In_2O_3$, P-$In_2O_3$, and R-$In_2O_3$ nanorods. (d) Corresponding EPR spectra of three $In_2O_3$ samples. (e) In K-edge XANES spectra of $In_2O_3$, P-$In_2O_3$, R-$In_2O_3$ nanorods, and reference samples. (f) Faradaic efficiencies of formate on three $In_2O_3$ catalysts. (g–i) Electronic localization function (ELF) of *HCOO on three $In_2O_3$ catalysts surfaces. (j) Gibbs free energy diagrams of $CO_2$-to-HCOOH over three catalysts. Reproduced with permission [92]. Copyright 2023, American Chemical Society.

ing to a high selectivity to $CO_2$ conversion to formate (Figs. 9g–j). Oxygen vacancies in the electrocatalyst can promote the adsorption and activation of $CO_2$ molecules and accelerate the electron transfer, thus improving the $CO_2$RR performance.

Various strategies have been used to enhance the $CO_2$RR performance on $In_2O_3$ catalysts, however, the real active site under electrocatalytic conditions is not well understood. Could the active site experience reversive transformation by the reaction intermediates or the O atoms during the reaction? The catalytic mechanism is kept or changed during the dynamic evolution of the active site is still unsolved. Therefore, it is essential to monitor the evolution of the catalyst and probe reaction intermediates and/or products on the catalyst surface by combining *in situ* characterization techniques and theoretical calculations.

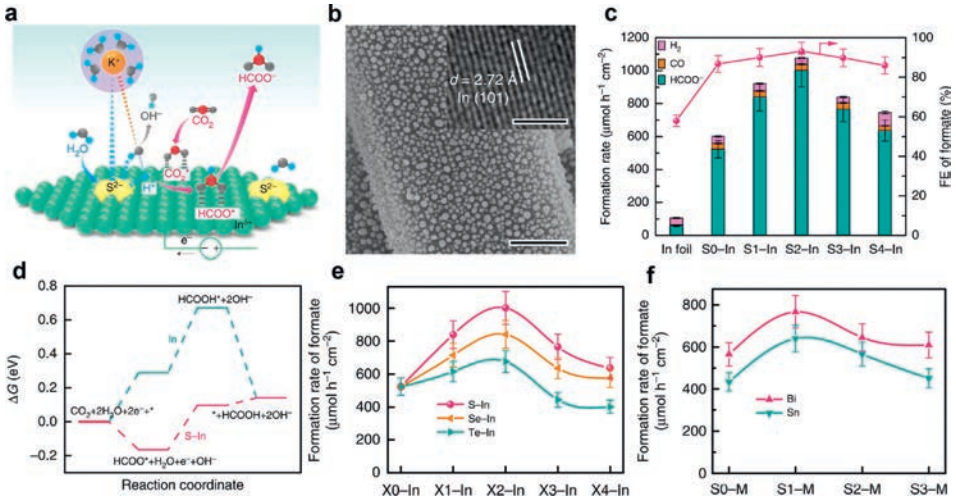


**Fig. 10.** (a) Schematic illustration showing the role of $S^{2-}$ in enhanced $CO_2$RR to formate *via* promoting the water dissociation and the fo rmation of H*. (b) SEM image of S−In catalyst (inset shows the HRTEM image). (c) Formation rates of different products, and FEs of formate on In foil and S−In catalysts. (d) Gibbs free energy diagrams for $CO_2$ reduction to formate on In (101) and S−In (101) surface. (e) Formation rates of formate on S−In, Se−In and Te−In catalysts. (f) Formation rates of formate over S−Bi and S−Sn catalysts. Reproduced with permission [94]. Copyright 2019, Springer Nature.

### 3.3.2. Doped $In_2O_3$

As a method to change the electronic structure of materials, element doping has been widely used in the field of semiconductors. The regulation of electronic structure can always tune the semiconductor performance by altering its band structure [93]. In the past decades, element doping has also received extensive attention in the field of electrocatalysis. It is generally believed that HER is a competing reaction of $CO_2$RR, and the promoted activation of $H_2O$ will reduce the Faradaic efficiency of $CO_2$RR products. However, Ma and his team broke this understanding and proposed that the activation of $H_2O$ molecules plays an important role in the reduction of $CO_2$ on their sulfur-doped In catalyst (Figs. 10a and b) [94]. In a wide range of 25–100 mA/cm$^2$, the $FE_{formate}$ on this catalyst can be maintained above 85%. The highest production rate can reach 1449 μmol h$^{-1}$ cm$^{-2}$ at a $FE_{formate}$ of 93% (Fig. 10c). DFT calculations indicated that the S doping can significantly reduce the formation energy of *HCOO on the catalyst surface (Fig. 10d). This doping effect is also effective when S was changed to other chalcogen elements such as selenium and tellurium or the metallic In was changed to other p-block metals (Bi, Sn), indicating that the doping is an effective route to promote the $H_2O$ molecules activation and further improve the electrocatalytic $CO_2$RR performance (Figs. 10e and f). In addition to nonmetal doping, metal doping of $In_2O_3$ catalyst for electrocatalytic $CO_2$RR has also been reported. Kim *et al.* found that monodispersed V-doped $In_2O_3$ nanocrystals with a staged octahedral shape exhibited unusual selectivity for $CO_2$ reduction to methanol, which was achieved by previously reported $In_2O_3$ catalysts [95]. Their results indicate that the V doping has a remarkable effect on the stabilization of intermediates, moving the reduction further and resulting in the generation of more reduced species (such as methanol).

Doping is a simple and outstanding method to modulate the electronic structure of electrocatalyst, and the $CO_2$RR performance can be significantly enhanced by a small amount of element doping. In the enhancement of the $CO_2$RR performance, doping works in two ways: (i) Accelerate electron transfer and improve the electric conductivity of electrocatalyst to improve catalytic activity; (ii) Adjust the adsorption energies of $CO_2$ molecules and the key reaction intermediates on the catalyst to improve the product selectivity. Therefore, the rational doping of the $In_2O_3$ catalyst could highly improve the $CO_2$RR performance.

### 3.3.3. $In_2O_3$-based heterojunction

It is well known that the construction of heterojunction interface can significantly alter the electron distribution of electrocatalyst and adjust the adsorption strength of reaction intermediates to improve the $CO_2$RR performance. Zhao *et al.* designed an $In_2O_3$/InN heterojunction and used it in electrolytic $CO_2$RR for the efficient production of formate for the first time [96]. They prepared the $In_2O_3$/InN heterojunction catalyst through a hydrothermal reaction together with a further annealing in $N_2/NH_3$ atmosphere. Their high-resolution TEM images showed that the as-synthesized heterojunction interface has well-defined lattice fringes, corresponding to (101) plane of hexagonal InN and (222) plane of cubic $In_2O_3$, respectively (Fig. 11a). They applied this $In_2O_3$/InN heterojunction catalyst for $CO_2$ reduction and found that the catalyst had a maximum $FE_{formate}$ of 95%. The $FE_{formate}$ could be maintained > 90% in a wide potential range between −1.37 V and −1.59 V (Fig. 11b). Electron localization function (ELF) analysis showed that the O atom in $In_2O_3$ and the N atom in InN could form a strong O-N coupling at the interface and offer a charge transfer channel for electron enrichment on InN surface (Fig. 11c). The Gibbs free energy change for $CO_2$RR to formate was further calculated to explore the role of the $In_2O_3$/InN heterojunction interface in the $CO_2$RR. The energy diagram shows that the $In_2O_3$/InN heterojunction can significantly strengthen the combination with $CO_2$ molecules and reduce the formation energy of the *HCOO intermediate, leading to the enhancement of the formate selectivity (Fig. 11d).

Apart from directly synthesizing electrocatalysts with heterojunction interfaces, *in situ* formation of heterojunction during electrolytic reactions is another effective way to enhance the catalytic activity of In-based catalysts. For example, Wulan *et al.* prepared the $In_2O_3$ catalyst by a fast Joule heating method and such $In_2O_3$ catalyst was *in situ* transformed into an In/$In_2O_3$ heterojunction catalyst during the $CO_2$ reduction to formate [97]. The introduction of the heterojunction interface can tune the electronic structure of In and accelerate the protonation process of the adsorbed bicarbonate species, leading to a high $FE_{formate}$ of 94%. The *in situ* experimental characterizations and theoretical calculations show that the In/$In_2O_3$ heterojunction catalyst can always maintain stable In-O species as real active sites under different electrolysis conditions (Figs. 11e and f).

The rational design of heterojunction catalyst through a feasible strategy to modulate the interfacial structures and properties is

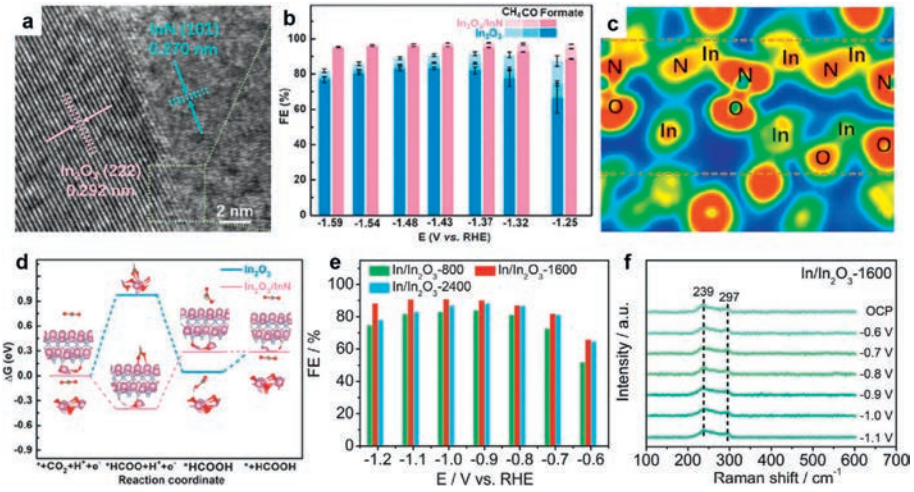


**Fig. 11.** (a) High-resolution TEM image of $In_2O_3$/InN heterojunction. (b) Faradaic efficiencies for formate, CO and $CH_4$ over $In_2O_3$ and $In_2O_3$/InN at different potentials. (c) Calculated electron localization function of $In_2O_3$/InN heterojunction. (d) Gibbs free energy diagram for $CO_2$RR to formate on the $In_2O_3$/InN heterojunction. Reproduced with permission [96]. Copyright 2022, Elsevier. (e) Faradaic efficiencies of formate on In/$In_2O_3$-800, In/$In_2O_3$-1600, In/$In_2O_3$-2400 catalysts. (f) Operando Raman spectra of In/$In_2O_3$-1600 with diffeerent applied potentials. Reproduced with permission [97]. Copyright 2022, Wiley-VCH GmbH.

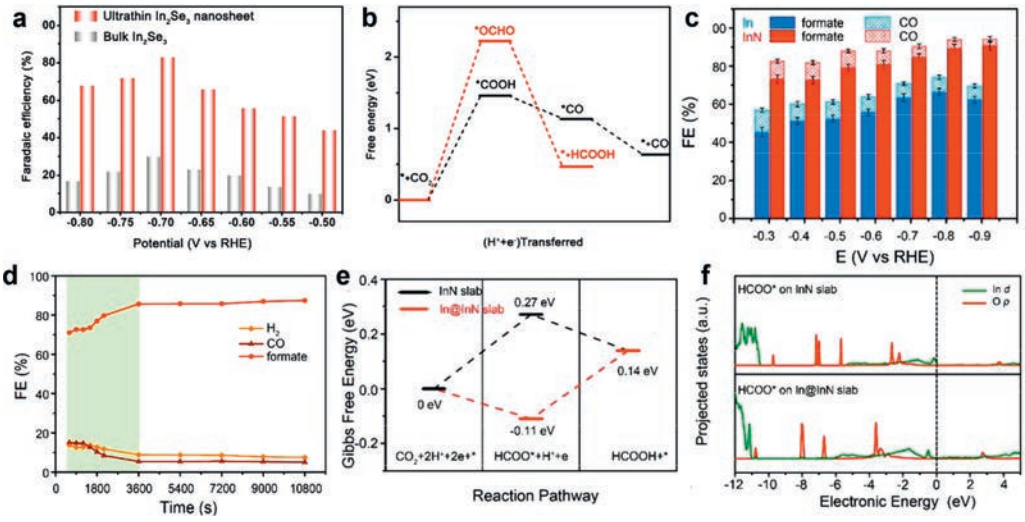


**Fig. 12.** (a) Faradaic efficiencies of CO on ultrathin $In_2Se_3$ nanosheet and bulk $In_2Se_3$ at different potentials. (b) Gibbs free energy diagrams of the formation of CO and HCOOH on $In_2Se_3$ (001) surface. Reproduced with permission [100]. Copyright 2019, Elsevier. (c) Faradaic efficiencies for different products over InN and In nanosheets at different applied potentials. (d) Faradaic efficiencies for different products over InN nanosheets at −0.9 V *vs.* RHE for 3 h. (e) Gibbs free energy diagrams of the formation of HCOOH on InN and In@InN slabs. (f) Projected density of states (PDOS) of HCOO* intermediates adsorbed on InN and In@InN slabs. Reproduced with permission [101]. Copyright 2020, American Chemical Society.

promising strategy to further improve the $CO_2$RR performance on $In_2O_3$ catalysts. However, revealing the structural evolution and real active sites of electrocatalysts during electrocatalytic reduction is challenging and of great significance to build the structure-activity relationship to further synthesize high-performance catalyst and to deeply understand the $CO_2$RR reduction mechanism.

### 3.4. Other indium-based catalysts

In addition to the catalysts mentioned above, indium sulfide or selenide-based composites have also been fabricated for electrocatalytic $CO_2$RR. Ning *et al.* prepared a GO supported $In_2S_3$ composite ($In_2S_3$-GO), which showed a high formate selectivity due to the high specific surface area and sufficient exposure of the (440) plane of $In_2S_3$ nanosheets [98]. Similarly, Liu *et al.* prepared the In nanoparticles-decorated $In_2S_3$ during the electrolytic $CO_2$RR [99]. The In–$In_2S_3$ hybrid catalyst showed a remarkable current density (for carbonaceous product) of 62.1 mA/cm$^2$ with a maximum $FE_{formate}$ of 76%. The improved catalytic activity was due to the increased carrier density and the lower work function after decoration of In nanoparticles, benefiting the $CO_2$ activation. $In_2Se_3$ catalyst has also been used for electrocatalytic $CO_2$RR, and the Faradaic efficiency of CO reaches 89% (Fig. 12a) [100]. DFT calculations suggested that the exposed Se atoms in $In_2Se_3$ could stabilize *COOH intermediates and thus boost the electrochemical performance of the $CO_2$-to-CO conversion (Fig. 12b). Moreover, Zhang *et al.* synthesized a highly efficient InN electrocatalyst which showed a FE of 95% for carbonaceous product (Figs. 12c and d) [101]. It was found that the InN was converted to an In-rich catalyst during the $CO_2$RR process. They proposed that the surface reconstruction resulted in a surface charge redistribution, significantly facilitating the adsorption of HCOO* and thus favoring the $CO_2$ reduction to formate (Figs. 12e and f).

## 4. Summary and outlook

In this review, we briefly reviewed the possible reaction pathways on In-based catalysts and the recently reported various In-based electrocatalysts were comprehensively and systematically summarized with a focus on their synthetic strategies, structures, catalytic performance, and reaction mechanisms. Strategies such as alloying, creating single-atom sites, element doping, heterojunction interface engineering, and defect engineering have significantly improved the catalytic performance of In-based catalysts for electrolytic $CO_2$RR. Nevertheless, there is still plenty of room to further develop highly efficient In-based catalysts for a wide range of practical and commercial applications. In future, more research focus should be paid on the economical production of stable In-based electrocatalyst, the deep understanding of dynamic active sites, and the potential industrialization of the electrolytic $CO_2$RR.

Firstly, most of the In-based catalysts suffered from complicated preparation processes. The development of a simple and scalable synthetic route to synthesize highly efficient In-based electrocatalysts is challenging but of significance for commercialization. The preparation strategies such as electroplating/electrodeposition, hydrothermal/solvothermal reaction, fast Joule-heating or the combination of these techniques might be helpful for large-scale production of stable In-based catalysts with low cost. Moreover, very few works have evaluated the long-term stability (>100 h) of In-based electrocatalysts; therefore, the chemical stability of In-based catalysts also needs further exploration to meet the industrial requirement for long-term electrolysis.

Secondly, the structure and chemical states of In-based electrocatalysts always change during the $CO_2$RR reduction process due to the applied large negative potentials and the possible transformation in the used electrolytes. To exactly identify the real active sites and correctly unveil the intrinsic reaction mechanism of electrolytic $CO_2$RR, *in situ* and/or *operando* characterizations techniques such as X-ray diffraction (XRD), electron paramagnetic resonance (EPR), Raman spectroscopy, attenuated total reflectance-Fourier transform infrared spectroscopy (ATR-FTIR), and X-ray absorption spectroscopy (XAS) should be used to monitor the phase/chemical state changes of In-based catalysts, the absorption/desorption of reaction intermediates during the electrolytic $CO_2$RR process. Meanwhile, the combination of theoretical calculation and *in situ* technique could be an effective way to deeply understand the reaction mechanism at the molecular level, and to provide a guidance for the rational design of highly-efficient electrocatalysts.

Finally, optimizing the cathode/anode reactions to improve energy utilization efficiency should also be considered. Specifically, the reactor design, the local environment, and $CO_2$ gas source should be optimized to improve the catalytic performance and reduce the cost. The current H-type cells always show limit current densities, and thus new types of electrolyzers, such as flow cells and membrane electrode assembly (MEA) systems, are needed to be further developed for practical applications. In addition, for liquid-phase products such as formic acid, the use of solid-state electrolytes is of significance because they can directly and effectively separate the liquid products during the $CO_2$RR process, greatly reducing the cost of product separation. Finally, the integration of $CO_2$-based battery devices to fulfill the high efficiency $CO_2$ utilization and conversion should also be developed.

## Declaration of competing interest

The authors declare that they have no known competing financial interests or personal relationships that could have appeared to influence the work reported in this paper.

## Acknowledgments

This work was supported by National Science Foundation of China (Nos. 22225606, 22261142663 and 22176029), the Excellent Youth Foundation of Sichuan Scientific Committee (No. 2021JDJQ0006).

## References

[1] D.Y.C. Leung, G. Caramanna, M.M. Maroto-Valer, Renew. Sustain. Energy Rev. 39 (2014) 426–443.
[2] W.H. Wang, Y. Himeda, J.T. Muckerman, et al., Chem. Rev. 115 (2015) 12936–12973.
[3] B. Deng, X. Zhao, Y. Li, et al., Sci. China Chem. 66 (2022) 78–95.
[4] L. Li, X. Li, Y. Sun, et al., Chem. Soc. Rev. 51 (2022) 1234–1252.
[5] K. Jiang, P. Ashworth, S. Zhang, et al., Renew. Sustain. Energy Rev. 119 (2020) 109601.
[6] J. Yu, J. Low, W. Xiao, et al., J. Am. Chem. Soc. 136 (2014) 8839–8842.
[7] J. Low, B. Cheng, J. Yu, Appl. Surf. Sci. 392 (2017) 658–686.
[8] Y. Zhao, G.I.N. Waterhouse, G. Chen, et al., Chem. Soc. Rev. 48 (2019) 1972–2010.
[9] A. Vasileff, Y. Zheng, S.Z. Qiao, Adv. Energy Mater. 7 (2017) 1700759.
[10] L. Zhang, Z.J. Zhao, J. Gong, Angew. Chem. Int. Ed. 56 (2017) 11326–11353.
[11] J. Wu, Y. Huang, W. Ye, et al., Adv. Sci. 4 (2017) 1700194.
[12] P. Gao, S. Li, X. Bu, et al., Nat. Chem. 9 (2017) 1019–1024.
[13] W. Li, H. Wang, X. Jiang, et al., RSC Adv. 8 (2018) 7651–7669.
[14] Y. Chen, C. Xu, S. Vaidyanathan, Appl. Energy 261 (2020) 114420.
[15] M. Bevilacqua, J. Filippi, H.A. Miller, et al., Energy Technol 3 (2015) 197–210.
[16] M. Jouny, W. Luc, F. Jiao, Ind. Eng. Chem. Res. 57 (2018) 2165–2177.
[17] Y. Zhai, P. Han, Q. Yun, et al., eScience 2 (2022) 467–485.
[18] J. Han, N. Wang, X. Li, et al., eScience 2 (2022) 623–631.
[19] K. Wang, D. Liu, L. Liu, et al., eScience 2 (2022) 518–528.
[20] Z. Zhu, Z. Li, J. Wang, et al., eScience 2 (2022) 445–452.
[21] Z.W. Seh, J. Kibsgaard, C.F. Dickens, et al., Science 355 (2017) eaad4998.
[22] J. Masa, C. Andronescu, W. Schuhmann, Angew. Chem. Int. Ed. 59 (2020) 15298–15312.
[23] Z. Zhang, M. Chi, G.M. Veith, et al., ACS Catal. 6 (2016) 6255–6264.
[24] G. Wen, D.U. Lee, B. Ren, et al., Adv. Energy Mater. 8 (2018) 1802427.
[25] X. Zhang, T. Lei, Y. Liu, et al., Appl. Catal. B 218 (2017) 46–50.
[26] W. Luc, C. Collins, S. Wang, et al., J. Am. Chem. Soc. 139 (2017) 1885–1893.
[27] Z. Chen, M.R. Gao, N. Duan, et al., Appl. Catal. B 277 (2020) 119252.
[28] J. Li, J. Jiao, H. Zhang, et al., ACS Sustain. Chem. Eng. 8 (2020) 4975–4982.
[29] S. Wang, B.Y. Guan, X.W.D. Lou, J. Am. Chem. Soc. 140 (2018) 5037–5040.
[30] M. Tahir, N.S. Amin, Appl. Catal. B 162 (2015) 98–109.
[31] F. Ye, J. Gao, Y. Chen, Y. Fang, Sustain. Energy Fuels 4 (2020) 3726–3731.
[32] W.J. Dong, C.J. Yoo, J.L. Lee, ACS Appl. Mater. Interfaces 9 (2017) 43575–43582.
[33] S. Wang, Z. Wu, C. Xu, et al., ACS Appl. Mater. Interfaces 14 (2022) 45423–45432.
[34] Y. Liang, W. Zhou, Y. Shi, et al., Sci. Bull. 65 (2020) 1547–1554.
[35] W. Yang, Y. Zhao, S. Chen, et al., Inorg. Chem. 59 (2020) 12437–12444.
[36] J. García, C. Jiménez, F. Martínez, et al., J. Catal. 367 (2018) 72–80.
[37] Y. Kwon, J. Lee, Electrocatalysis 1 (2010) 108–115.
[38] Y. Li, Y. Jin, X. Zong, et al., J. Mater. Chem. A 11 (2023) 11445–11453.
[39] K. Yao, H. Wang, X. Yang, et al., Appl. Catal. B 311 (2022) 121377.
[40] T. Ren, Z. Miao, L. Ren, et al., Small 19 (2023) 2205168.
[41] M. Yu, P.F. Sui, X.Z. Fu, et al., Adv. Energy Mater. 13 (2023) 2203191.
[42] N. Han, P. Ding, L. He, et al., Adv. Energy Mater. 10 (2020) 1902338.
[43] D. Xia, H. Yu, H. Xie, et al., Nanoscale 14 (2022) 7957–7973.
[44] R. Kortlever, J. Shen, K.J.P. Schouten, et al., J. Phys. Chem. Lett. 6 (2015) 4073–4082.
[45] A.A. Peterson, F. Abild-Pedersen, F. Studt, et al., Energy Environ. Sci. 3 (2010) 1311–1315.
[46] H.A. Hansen, J.B. Varley, A.A. Peterson, et al., J. Phys. Chem. Lett. 4 (2013) 388–392.
[47] J.T. Feaster, C. Shi, E.R. Cave, et al., ACS Catal. 7 (2017) 4822–4827.
[48] S. Nitopi, E. Bertheussen, S.B. Scott, et al., Chem. Rev. 119 (2019) 7610–7672.
[49] C. Xiao, J. Zhang, ACS Nano 15 (2021) 7975–8000.
[50] J. He, N.J.J. Johnson, A. Huang, et al., ChemSusChem 11 (2018) 48–57.
[51] H. Xiang, S. Rasul, B. Hou, et al., ACS Appl. Mater. Interfaces 12 (2020) 601–608.
[52] W. Luo, W. Xie, R. Mutschler, et al., ACS Catal. 8 (2018) 6571–6581.
[53] O. Martin, A.J. Martín, C. Mondelli, et al., Angew. Chem. Int. Ed. 55 (2016) 6261–6265.
[54] M. Zhu, P. Tian, J. Li, et al., ChemSusChem 12 (2019) 3955–3959.
[55] S. Rasul, D.H. Anjum, A. Jedidi, et al., Angew. Chem. Int. Ed. 54 (2015) 2146–2150.
[56] A. Jedidi, S. Rasul, D. Masih, et al., J. Mater. Chem. A 3 (2015) 19085–19092.
[57] C. Shen, P. Wang, L. Li, et al., Nano Res. 15 (2021) 528–534.
[58] Q. Xie, G.O. Larrazábal, M. Ma, et al., J. Energy Chem. 63 (2021) 278–284.
[59] Z.B. Hoffman, T.S. Gray, K.B. Moraveck, et al., ACS Catal. 7 (2017) 5381–5390.
[60] S. Ma, M. Sadakiyo, M. Heima, et al., J. Am. Chem. Soc. 139 (2017) 47–50.
[61] P. Wang, M. Qiao, Q. Shao, et al., Nat. Commun. 9 (2018) 4933.
[62] L.C. Pardo Pérez, D. Teschner, E. Willinger, et al., Adv. Funct. Mater. 31 (2021) 2103601.

[63] J. Wang, S. Ning, M. Luo, et al., Appl. Catal. B 288 (2021) 119979.
[64] G.O. Larrazábal, A.J. Martín, S. Mitchell, et al., ACS Catal. 6 (2016) 6265–6274.
[65] D. Tan, W. Lee, Y.E. Kim, et al., ACS Appl. Mater. Interfaces 14 (2022) 28890–28899.
[66] G.O. Larrazábal, A.J. Martín, S. Mitchell, et al., J. Catal. 343 (2016) 266–277.
[67] D. Pavesi, F. Dattila, R.C.J. Van de Poll, et al., J. Catal. 402 (2021) 229–237.
[68] L. Liu, H. Akhoundzadeh, M. Li, et al., Small Methods 31 (2023) 2300482.
[69] Y. Wang, T. Liu, Y. Li, Chem. Sci. 13 (2022) 6366–6372.
[70] W. Guo, X. Tan, J. Bi, et al., J. Am. Chem. Soc. 143 (2021) 6877–6885.
[71] X. Zu, X. Li, W. Liu, et al., Adv. Mater. 31 (2019) 1808135.
[72] H. Zhang, J. Li, S. Xi, et al., Angew. Chem. 58 (2019) 14871–14876.
[73] M. Huang, B. Deng, X. Zhao, et al., ACS Nano 16 (2022) 2110–2119.
[74] S. Li, S. Zhao, X. Lu, et al., Angew. Chem. Int. Ed. 60 (2021) 22826–22832.
[75] N. Zhang, X. Zhang, L. Tao, et al., Angew. Chem. Int. Ed. 60 (2021) 6170–6176.
[76] Q. He, J.H. Lee, D. Liu, et al., Adv. Funct. Mater. 30 (2020) 2000407.
[77] J. Zhang, G. Zeng, L. Chen, et al., Nano Res. 15 (2022) 4014–4022.
[78] S. Li, X. Lu, S. Zhao, et al., ACS Catal. 12 (2022) 7386–7395.
[79] H. Shang, T. Wang, J. Pei, et al., Angew. Chem. Int. Ed. 59 (2020) 22465–22469.
[80] P. Lu, X. Tan, H. Zhao, et al., ACS Nano 15 (2021) 5671–5678.
[81] Z. Zhang, J. Zhu, S. Chen, et al., Angew. Chem. Int. Ed. 62 (2023) e202215136.
[82] J. Yuan, Y. Chen, F. Liu, et al., Catal. Commun. 177 (2023) 106640.
[83] Z. Fan, R. Luo, Y. Zhang, et al., Angew. Chem. Int. Ed. 62 (2023) e202216326.
[84] Z. Liang, L. Song, M. Sun, et al., Nano Res. 16 (2023) 8757–8764.
[85] Z. Liang, L. Song, M. Sun, et al., Sci. Adv. 7 (2021) eabl4915.
[86] C.W. Li, M.W. Kanan, J. Am. Chem. Soc. 134 (2012) 7231–7234.
[87] R. Kas, R. Kortlever, A. Milbrat, et al., Phys. Chem. Chem. Phys. 16 (2014) 12194–12201.
[88] Y. Huang, X. Mao, G. Yuan, et al., Angew. Chem. Int. Ed. 60 (2021) 15844–15848.
[89] Z. Zhang, F. Ahmad, W. Zhao, et al., Nano Lett. 19 (2019) 4029–4034.
[90] B. Pan, G. Yuan, X. Zhao, et al., Small Sci. 1 (2021) 2100029.
[91] J. Zhang, R. Yin, Q. Shao, et al., Angew. Chem. Int. Ed. 58 (2019) 5609–5613.
[92] Q. Cheng, M. Huang, L. Xiao, et al., ACS Catal. 13 (2023) 4021–4029.
[93] D. Dvoranová, V. Brezová, M. Mazúr, et al., Appl. Catal. B 37 (2002) 91–105.
[94] W. Ma, S. Xie, X.G. Zhang, et al., Nat. Commun. 10 (2019) 892.
[95] M.G. Kim, J. Jeong, Y. Choi, et al., ACS Appl. Mater. Interfaces 12 (2020) 11890–11897.
[96] X. Zhao, M. Huang, B. Deng, et al., Chem. Eng. J. 437 (2022) 135114.
[97] B. Wulan, X. Cao, D. Tan, et al., Adv. Funct. Mater. 33 (2023) 2209114.
[98] H. Ning, X. Fei, Z. Tan, et al., ACS Appl. Nano Mater. 5 (2022) 2335–2342.
[99] X. Yuan, Y. Luo, B. Zhang, et al., Chem. Commun. 56 (2020) 4212–4215.
[100] F. Lü, G. Qi, X. Liu, et al., Electrochem. Commun. 103 (2019) 127–132.
[101] A. Zhang, Y. Liang, H. Li, et al., Nano Lett. 20 (2020) 8229–8235.